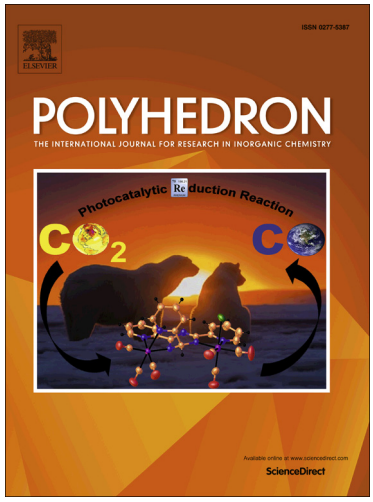

Synthesis of nuclear waste simulants by reaction precipitation: Formation of caesium phosphomolybdate, zirconium molybdate and morphology modification with citratomolybdate complex

Neepa Paul, Robert B. Hammond, Timothy N. Hunter, Michael Edmondson, Lisa Maxwell, Simon Biggs

PII: S0277-5387(14)00795-5
DOI: http://dx.doi.org/10.1016/j.poly.2014.12.030
Reference: POLY 11118

To appear in: *Polyhedron*

Received Date: 17 October 2014
Accepted Date: 26 December 2014

Please cite this article as: N. Paul, R.B. Hammond, T.N. Hunter, M. Edmondson, L. Maxwell, S. Biggs, Synthesis of nuclear waste simulants by reaction precipitation: Formation of caesium phosphomolybdate, zirconium molybdate and morphology modification with citratomolybdate complex, *Polyhedron* (2015), doi: http://dx.doi.org/10.1016/j.poly.2014.12.030

Synthesis of nuclear waste simulants by reaction precipitation: Formation of caesium phosphomolybdate, zirconium molybdate and morphology modification with citratomolybdate complex

Neepa Paul[a], Robert B. Hammond[a] Timothy N. Hunter[a,*], Michael Edmondson[b], Lisa Maxwell[c] and Simon Biggs[a,d]

[a] *Institute of Particle Science and Engineering, School of Chemical and Process Engineering, The University of Leeds, Leeds, LS2 9JT, UK*
[b] *National Nuclear Laboratory, Central Laboratory, Sellafield, Seascale, Cumbria, CA20 1PG, UK*
[c] *Sellafield Ltd, Sellafield, Seascale, Cumbria, CA20 1PG, UK*

[d] *Faculty of Engineering, Architecture & Information Technology, The University of Queensland, Brisbane, QLD 4072, AU*

Abstract

Caesium phosphomolybdate ($Cs_3PMo_{12}O_{40} \cdot xH_2O$) and zirconium molybdate ($[ZrMo_2O_7(OH)_2] \cdot 2H_2O$) solids are known to precipitate out from highly active liquors (HAL) during reprocessing of spent nuclear fuel. Here, a new synthesis for these simulants is reported; with the initial step producing spherical ceasium phosphomolybdate particles, which can then be converted into cubic Zirconium molybdate. Additionally, the addition of citric acid prior to the formation of the zirconium salt is investigated. In this case, a citratomolybdate complex is generated, leading to the synthesis of elongated cuboidal zirconium citratomolybdate ($[ZrMo_2O_7(OH)_2] \cdot 2H_2O \cdot [(MoO_2)_2O(cit)_2]$). A key focus of this study is to explore the optimisation of reaction conditions to create a controlled environment for the particles to form with high conversion rates and with desired shape properties. Elemental and structural characterisation of the particles at various points during the synthesis, as well as post-synthesis, was undertaken to provide further insights. Ultimately, it is of importance to determine the mechanism of how these simulants are formed within the components in HAL. Establishing the influence of particle properties on HAL behaviour is key for current processing, post operational clean out (POCO) and life-time assessment of the nuclear waste facilities.

* Corresponding author: Tel: +44 113 343 2790; Email: T.N.Hunter@leeds.ac.uk

1. Introduction

Caesium phosphomolybdate ($Cs_3PMo_{12}O_{40} \cdot xH_2O$, "Cs-phosphomolybdate") and zirconium molybdate ($[ZrMo_2O_7(OH)_2] \cdot 2H_2O$, "Zr-molybdate") are important nuclear waste particulate systems, also known as Highly Active Liquor (HAL) solids created in fuel reprocessing cycles. Synthesis of the HAL simulants through non-radioactive chemical precursors, provide an insight into the chemical mechanism for particle formation and opportunities for synthesis modification. During the reprocessing of spent nuclear fuel, useful uranium and plutonium components are removed by solvent extraction recycling. The remaining fission products (which are dissolved in nitric acid) are then concentrated in evaporators. It is at this stage where the precipitation of Cs-phosphomolybdate and Zr-molybdate are most likely to occur, due to the high concentrations of zirconium, caesium and molybdenum ions.

It is important in the laboratory, to replicate the conditions (i.e. acidity and temperature) in which these HAL solids form as closely as possible, allowing for the production of relevant simulants for comparative studies. Post-operational clean out (POCO) procedures for the highly-active storage tanks (HASTs) will require the complete removal of solids from inside the vessels and associated pipework. At this point additives may be introduced, where morphological manipulation of the Zr-molybdate particles is advantageous for subsequent processing. A primary objective of this current research is to study resulting changes to particle shape and crystal structure for zirconium complexes formed with such additives.

A number of studies have been carried out to understand the formation of Zr-molybdate [1-5], while in contrast, relatively few have detailed synthesis routes for Cs-phosphomolybdate [6, 7]. Formation of Cs-phosphomolybdate is conducted using nitric acid solutions with various concentrations of caesium ions and phosphomolybdic acid, with reaction conditions maintained at 70^{o}C under continuous agitation. It is believed $Cs_3PMo_{12}O_{40} \cdot xH_2O$ is formed

by the substitution of hydrated hydrogen ions with caesium ions [7], where *x* can range from 9 to 14 H_2O depending, on the drying method [6].

Various techniques for Zr-molybdate synthesis have been developed originating from the sol-gel precipitation method by Clearfield & Blessing [1]. Generally, most methodologies based on this work result in the production of $[ZrMo_2O_7(OH)_2] \cdot 2H_2O$, formally known as zirconium molybdenum dihydroxide dihydrate. The reported synthesis required the preparation of aqueous reactant solutions of 200 mL 0.5 M zirconium oxide dichloride octahydrate, $ZrOCl_2(H_2O)_8$ and 200 ml of 1M sodium molybdate, $Na_2MoO_4(H_2O)_2$, producing a white crystalline powder.

The mechanism of Zr-molybdate formation may be influenced by a number of additional species found in liquors from nuclear fuel reproccessing. Xuegang *et al.* [2] created a simulant precipitation liquor containing 15 elements at different concentrations. The production of $[ZrMo_2O_7(OH)_2] \cdot 2H_2O$ was found to be dependent on the Mo/Zr contained within the simulated high level waste, thus the highest concentration levels of zirconium and molybdenum were implemented. The composition of aqueous solutions chosen closely resembled those present in nuclear fuel reprocessing plants. A further study by Magnaldo *et al.* [8] explored the nucleation and growth properties of Zr-molybdate crystals to determine a possible mechanism for the formation fouling layers, which may compromise the integrity of the nuclear waste facilities. It was found that deposition of Zr-molybdate from bulk fluid can occur in addition to localised surface nucleation, forming extended surface networks with the ability to create a fouling layer including other debris.

Other methods of Zr-molybdate synthesis involve oxidation catalytic methods [3], while Monray-Guzman and co-workers have discussed the production of Zr-molybdate gel and its

effect on Mo/Tc generators [4, 9, 10]. Kumar *et al*. [11] studied the potential of separation of long-lived radionuclide such as ^{137}Cs and ^{90}Sr, where the sorption behaviour a on zirconium molybdate was investigated. Again, a sol-gel method was implemented to produce $[ZrMo_2O_7(OH)_2] \cdot 2H_2O$ using ammonium molybdate and zirconium oxychloride. Ultimately, the sorption of ^{137}Cs on was more likely than ^{90}Sr, indicating how precipitation of these salts in a HAL environment may affect concentration of other mobile ions present. Other applications include the use of thermal expansion materials [12, 13].

A key feature in the synthesis of Zr-molybdate, is the interaction of the molybdenum and additives, such as citric acid, to produce citratomolybdate complexes, which are commonly used for analytical applications and in corrosion resistant alloys [14]. The citratomolybdate complex has been identified in numerous studies [15-18]. Alcock *et al.* synthesised $K_4[Mo_4O_{11}(cit)_2]6H_2O$, where the complex anion was determined using XRD [16]. The structure of the complex contains a central oxygen atom bound to two molybdenum atoms. Each of the molybdenum atoms are octahedral coordinated, and the tridenate citric acid ligands are bound to the molybdenum atoms. The citric acid OH and O atoms of the carboxylate groups form covalent bonds with the molybdenum atoms. The central oxygen atom essentially creates an oxygen bridge, Mo-O-Mo, where the citratomolybdate complex is cis-bound with two citrate ligands.

Currently, there is only limited information is available on influence of the citratomolybdate complex on the crystal formation of zirconium molybdate. Additionally, a unique approach will be explored here, by which Zr-molybdate is produced using caesium phosphomolybdate dispersions as the foundation for molybdate ion liberation. Ultimately, this research will highlight novel synthetic routes for the formation of these highly active nuclear waste simulants, as well as the morphological manipulation of Zr-molybdate to produce zirconium

citratomolybdate, from the addition of citric acid. A current interest in the UK nuclear industry is to find viable routes to modify the morphology of the precipitated zirconium salts, as one approach to improve their processing and eventual disposal. Further, this study will focus on optimising synthesis methodology, to produce a high yield, uniform batch of morphological specific products.

2. Materials & Methods

2.1 Materials

The three materials synthesised in this study were caesium phosphomolybdate ($Cs_3PMo_{12}O_{40} \cdot xH_2O$), zirconium molybdate ($[ZrMo_2O_7(OH)_2] \cdot 2H_2O$) and zirconium citratomolybdate ($[ZrMo_2O_7(OH)_2] \cdot 2H_2O \cdot [(MoO_2)_2O(cit)_2]$). Table 1 provide key information for all of the required reagents used in the study for the production of these species.

Table 1 Materials used for analytical measurements and raw materials required for synthesis

Compound	Chemical Name	Formula	Purity/ Concentration	Supplier
Dodecamolybdophosphoric acid	Phosphomolybdic acid	$H_3PMo_{12}O_{40}$	80%	ACROS Organics
Caesium nitrate		$CsNO_3$	99.8%	Alfer Aesar
Zirconium(IV) oxynitrate	Zirconyl nitrate	$ZrO(NO_3)_2$	212 g/L	Johnson and Matthey
3-carboxy-3-hydroxypentanedioic acid	Citric acid	$C_6H_8O_7$	99.8%	Fisher Scientific
Nitric acid		HNO_3	70% (16M)	Fisher Scientific

2.2 Particle synthesis

The synthesis of the chosen nuclear waste simulant particles was carried out in a batch reactor vessel, with a set-up as illustrated in Figure 1.

Figure 1: A 4 L Batch reactor vessel set-up for caesium phosphomolybdate, zirconium molybdate and zirconium citratomolybdate synthesis. The reactor vessel is a jacketed vessel (containing silicon oil for heating purposes) an overhead paddle agitator, a condenser with circulating water at 5°C and a temperature probe.

2.2.1 Synthesis of caesium phosphomolybdate ($Cs_3PMo_{12}O_{40} \cdot xH_2O$)

Synthesis of Cs-phosphomolybdate involved preparing phosphomolybdic acid ($H_3PMo_{12}O_{40}$) and caesium nitrate ($CsNO_3$) solutions. The method was established from an internally circulated document within the National Nuclear Laboratory (NNL), and is similar to the reported work of Bykhovskii and co-workers [7]. Phosphomolybdic acid and caesium nitrate solutions were individually prepared by dissolving the solids, at a ratio of 3:1 $H_3PMo_{12}O_{40}$ (242 g) to $CsNO_3$ (82 g), in 2 M nitric acid under continuous stirring. Preparation of these solutions was carried out separately in two individual 2 L beakers, where the solids were stirred until they were fully dissolved, at room temperature. The caesium nitrate was then dispensed into the empty 4 L reactor vessel, illustrated in figure 1, and heated to 50°C. Phosphomolybdic acid was added at a rate of 16.67 mL/min to the $CsNO_3$ over a 1 hr period, using a 20 mL syringe. Following the complete addition of the acid, the solution was maintained at 50°C with continuous stirring (approximately 200 rpm).

Yellow Cs-phosphomolybdate precipitated out during the 48 hrs reaction period. Separation of the solids from the mother liquor was achieved by decanting. The final dispersion was left to stand for 1 hr, after which phase separation of the solids was achieved and a clear supernatant produced. The removal of the supernatant required a hand pump. The remaining solids were collected and oven dried at 50°C for 48 hrs, and the solids did not require a cleaning step. The complete synthesis protocol for $Cs_3PMo_{12}O_{40} \cdot xH_2O$ is shown in Figure 2.

2.2.2 Synthesis of zirconium molybdate ($[ZrMo_2O_7(OH)_2] \cdot 2H_2O$)

The zirconium molybdate synthesis was also derived from an internal report from NNL, and was based on that reported by Clearfield and Blessing [1]. The method implemented in this

research however provides an alternative to the sodium molybdate compound used in the earlier research, and instead uses the produced Cs-phosphomolybdate as a reagent. Synthesis required the initial conditioning of 397 mL zirconyl nitrate ($ZrO(NO_3)_2$) dissolved in 6 M nitric acid at 100 °C. This was carried out in a 1 L round bottomed flask, under reflux. Initially, the zirconyl nitrate dispersion gives a milky-white appearance when added to nitric acid. Conditioning at 100°C allows breakdown of the compound to produce $[Zr]^{4+}$ ions. The solution was left to cool down to room temperature prior to the $[ZrMo_2O_7(OH)_2] \cdot 2H_2O$ synthesis.

A 2 L Cs-phosphomolybdate suspension using 121 g of $H_3PMo_{12}O_{40}$ and 41 g of $CsNO_3$ was firstly synthesised in the 4 L reactor vessel (as per Section 2.2.1). After 48 hrs, the suspension was heated up to 90 °C. The dissolved zirconyl nitrate solution was then added at a rate of 16.67 mL/min over a 1 hr period with continuous stirring (~200 rpm) whilst the reaction medium was maintained at 90 °C under reflux. The experimental set-up was again as shown in Figure 1.

Conversion of Cs-phosphomolybdate to Zr-molybdate can be a lengthy process, sometimes taking up to 14 days. The conversion is visually monitored by an associated characteristic colour change from yellow to white. Once again, at the conclusion of the reaction, the precipitated $[ZrMo_2O_7(OH)_2] \cdot 2H_2O$ solids were left to naturally settle and the liquor was decanted. The solids were washed once with 2 M nitric acid to remove excess zirconium, and extracted solids required oven drying at 50°C. The overall synthesis method is illustrated in Figure 2.

Figure 2: Schematic illustration of the synthesis steps for caesium phosphomolybdate and zirconium molybdate particle production.

2.2.3 Synthesis of zirconium citratomolybdate – Method 1

This research explored two types of zirconium molybdate, to understand the changes to particle characteristics associated with morphological transformation. Elongation of the particles required the synthesis to be modified with an organic additive, citric acid. As discussed within the introduction, the citric acid is known to form a citratomolybdate complex [15-18], this initiated the interest in the influence of the complex interaction with $[ZrMo_2O_7(OH)_2] \cdot 2H_2O$.

Initially, a simple zirconium citratomolybdate ($[ZrMo_2O_7(OH)_2] \cdot 2H_2O \cdot [(MoO_2)_2O(cit)_2]$) synthesis method was investigated, which required only the addition of citric acid simultaneously with the zirconyl nitrate over a period of 1 hr to the Cs-phosphomolybdate conversion (as described in Section 2.2.2). 20 mol% of the citric acid was added to the synthesis and conditions set as per the $[ZrMo_2O_7(OH)_2] \cdot 2H_2O$ method. The reaction was kept at 90 ^{o}C for 336 hrs under reflux with continuous stirring at 200 rpm. The same cleaning procedure with nitric acid was undertaken also as with the Zr-molybdate synthesis.

The overall synthesis method 1 of zirconium citratomolybdate is illustrated in Figure 3.

Figure 3: A schematic of method 1 illustrating the synthesis steps required for morphological modification of zirconium molybdate to produce zirconium citratomolybdate particles with incorporation of citric acid.

2.2.4 Synthesis of zirconium citratomolybdate – Method 2

Initial experiments with Method 1 gave an overall poor conversion of the Cs-phosphomolybdate to zirconium citratomolybdate (see Section 3.3 discussion) and thus a modified method, illustrated in Figure 4, was implemented to improve the conversion. The optimised synthesis method, in contrast to the initial Method 1, required the change in the citric additive induction time to *t = 30 mins*, a change in additive flow rate to 3.34 mL/min and the addition of a washing step. The intent was to optimise the key parameters to improve

the overall yield conversion achieved in Method 1, where the reasoning will be further discussed in Section 3.4. The reaction was again kept at 90 ^{o}C under reflux with continuous stirring at 200 rpm. Post filtration, it was necessary to wash the Zr-citratomolybdate product with ammonium carbamate ($NH_2CO_2NH_4$), which was undertaken to dissolve any excess Cs-phosphomolybdate and to generate a high yield of uniform $[ZrMo_2O_7(OH)_2] \cdot 2H_2O \cdot [(MoO_2)_2O(cit)_2]$ particles.

The overall synthesis Method 2 of zirconium citratomolybdate is illustrated in Figure 4.

Figure 4: Schematic of Method 2 illustrating the synthesis steps require for morphological transformation of zirconium molybdate to zirconium citratomolybdate with incorporation of citric acid.

3 Results and discussion

3.1 Synthesis of Caesium phosphomolybdate ($Cs_3PMo_{12}O_{40} \cdot xH_2O$)

Caesium phosphomolybdate formation is a double replacement reaction, where both the reactants, phosphomolybdic acid ($H_3PMo_{12}O_{40}$) and caesium nitrate ($CsNO_3$) dissociate, with $[PMo_{12}O_{40}]^{3-}$ and $[H]^{+}$ ions forming from the phosphomolybdic acid while $[Cs]^{+}$ and $[NO_3]^{3-}$ ions dissociate from the caesium nitrate. The proposed formation is based on the molecular formula, chemical structure and the initial quantities of raw materials, and is expressed by the following stoichiometric equation:

$$H_3PMo_{12}O_{40} \cdot 14H_2O_{(aq)} + 3CsNO_{3(aq)} \rightarrow Cs_3PMo_{12}O_{40} \cdot 14H_2O_{(s)} + 3HNO_{3_{(aq)}} \quad \text{Equation 1}$$

With a net ionic precipitate reaction:

$$[PMo_{12}O_{40} \cdot 14H_2O]^{3-}{}_{(aq)} + [Cs]^{+}_{(aq)} \rightarrow Cs_3PMo_{12}O_{40} \cdot 14H_2O_{(s)} \quad \text{Equation 2}$$

This reaction produced a conversion of 94% after 48 hrs, with constant temperature and agitation speed. The precipitated solids, when separated from the liquor and dried, produced a

crystalline product with a bright yellow appearance. Figure 5 illustrates SEM images of the Cs-phosphomolybdate post-synthesis.

Figure 5: Scanning electron microscope images of synthesised caesium phosphomolybdate particles. Images are taken at different magnifications: (a) 23.01 K; (b) 23.25 K ; (c) 29.32 K; (d) 151.09 K .

The SEM images in Figure 5 show the synthesised Cs-phosphomolybdate sample to be submicron, near size monodisperse, spherical particles. The primary particle size is ~200 nm with a range of larger aggregates having sizes of ~1 µm. With an increase in magnification to 151.09 K it appears that the 200 nm particles are polycrystalline and themselves consist of smaller spherical particles, identified by the roughened surfaces of the primary aggregate. Figure 6 illustrates a proposed mechanism of Cs-phosphomolybdate aggregate formation.

Figure 6: Proposed aggregation mechanism for caesium phosphomolybdate particles. Stage 1: formation of the nanocrystallites; Stage 2: formation of the primary aggregates, consisting of cemented nanocrystallites; Stage 3: formation of the secondary aggregate, consisting of the submicron aggregates

The proposed mechanism in Figure 6 suggests there are three distinct stages in the formation of the overall Cs-phosphomolybdate particles. In Stage 1, nanocrystallites are formed (the size of which has not been defined); in Stage 2 the attractive van dan der Waals forces in the system causes the aggregation of these nanocrystallites and the formation of a primary spherical aggregate with a size of ~200 nm (illustrated in figure 5 (c)); and, in Stage 3 the primary aggregates themselves form larger secondary aggregates, with an overall size of a few microns.

3.2 Synthesis of zirconium molybdate

It may be expected that the initial step of Zirconium molybdate formation is the breakdown of Cs-phosphomolybdate at high temperatures, which leads to the formation of the

oxomolybdate complex, $[Mo_2O_5]^{2+}$. The assumption is based on research conducted by Zhou *et al.* [17,18]. Upon liberation, this complex reacts with the $[Zr]^{+}$ released from the conditioned zirconyl nitrate ($ZrO(NO_3)_2$). It is this reaction between the oxomolybdate and zirconyl nitrate which produces Zr-molybdate particles. The proposed formation of $[ZrMo_2O_7(OH)_2] \cdot 2H_2O$, based on the molecular formula, chemical structure and the initial quantities of raw materials, is expressed by the following stoichiometric equation

$$Cs_3PMo_{12}O_{40} \cdot 14H_2O_{(aq)} + 6ZrO(NO_3)_{2(aq)} + 3HNO_{3(aq)} + 10H_2O_{(aq)} \rightarrow 6[ZrMo_2O_7(OH)_2] \cdot 2H_2O_{(s)} + H_3PO_{4(aq)} + 3CsNO_{3(aq)} + 9H_2O_{(aq)} \quad \text{Equation 3}$$

With a net ionic precipitate reaction:

$$[PMo_{12}O_{40}]^{3-}_{(aq)} + [Zr]^{+}_{(aq)} \rightarrow [ZrMo_2O_7(OH)_2] \cdot 2H_2O_{(s)} \quad \text{Equation 4}$$

This reaction produced a conversion of 84% after 48 hrs, at constant temperature and agitation speed. The precipitated solids separated from the liquor and dried produced a crystalline product with a cream/white appearance. SEM images of the Zr-molybdate particles are illustrated in Figure 7.

Figure 7: Scanning electron microscope images of synthesised zirconium molybdate particles. Images are taken at different magnifications: (a) 1.74 K; (b) 7.79 K; (c) 19.66 K; (d) 27.99 K.

The SEM images, in Figure 7, illustrate that basic particle shape of Zr-molybdate to be cubic. Individual particle sizes range from approximately 500 nm to 3µm. Figure 7(c) and (d) show the presence of finer particles in addition to the larger 3 µm $[ZrMo_2O_7(OH)_2] \cdot 2H_2O$ particles, this is indicative of some moderate size polydispersity; however the majority of particles were of a size order between 1 – 5 µm.

Figure 7 (c) shows evidence of multiple penetration twinning, where crystals are formed by growth and pass through each other. There are various mechanisms associated with the

incorporation of growth units to form penetration twins, where the crystal units seem to grow simultaneously but independent of each other [19]. A proposed mechanism for multiple twinning Zr-molybdate morphologies is a change in the lattice during formation, which can be due to a substituting growth unit. In this case both $[Mo_2O_5]^{2-}$ and $[Zr]^{+}$ are the crystal nuclei which exist in solution. Substitution of a large ion takes place along the c-axis and the incorporation of the growth units on growth interfaces (0 0 4) or (0 0 $\bar{4}$), this results in the formation of a twinned crystals [20]. Multiple penetration twinning occurs when two or more structures contain interpenetrating lattice and therefore occur in pairs. As the planes of symmetry are identical, the crystals units pass through each other during growth [21].

For both Cs-phosphomolybdate and Zr-molybdate production, considering the initial quantity of the molybdate compound, it can be concluded that the concentration of $[Mo_2O_5]^{2-}$ ions released in solution controls the rate of reaction and ultimately the yield of solid produced. It is therefore of importance to control the release of the $[Mo_2O_5]^{2-}$ complex to obtain the desired solid product. This will be further discussed later in the paper.

3.3 Staged synthesis of zirconium citratomolybdate with Method 1

The conversion of Cs-phosphomolybdate to zirconium citratomolybdate proved to be challenging, and detailed characterisation was required to fully understand the mechanism. Throughout the $[ZrMo_2O_7(OH)_2] \cdot 2H_2O \cdot [(MoO_2)_2O(cit)_2]$ synthesis, 2 mL aliquots were extracted at 24 hr, 192 hr and 330 hr intervals to understand how the material changed during conversion. The samples were analysed by SEM imaging to observe the morphological changes at varying stages of the reaction.

Figure 8: Scanning electron images illustrating the breakdown of caesium phosphomolybdate, 24 hrs into the synthesis. The images were taken at different magnifications: (a) hollow centre crystal at 130.56 K; (b) filled centre crystal at 152.60 K.

Initial SEM images in Figure 8 of Cs-phosphomolybdate shows smooth surfaces of the polycrystalline crystals. After approximately 24 hrs, it can be seen that the Cs-phosphomolybdate breaks down, due to the increase of temperature from 50 to 90^{o}C [22]. The aggregates are shown to dissolve and form a hollow centre, indicated by green arrows in Figure 8(a), and in some cases as shown in Figure 8(b), a crystalline Cs-phosphomolybdate surface (yellow arrow) with an increased core density (red arrow). Hollow spheres are produced by Ostwald ripening or differential diffusion within the solid spheres [23-25]. In the latter case, the breakdown of the Cs-phosphomolybdate releases reagents causing the solution concentration to increase past their supersaturation point. This is an ideal environment for spontaneous nucleation to occur and causes a secondary layer of crystalline Cs-phosphomolybdate on the outside of the initial surface. Contingent to the production of a diffusion pathway through the outer crystalline layer, the inner core dissolves. At this stage, the supersaturation rate increases in solution again, above the solubility of Cs-phosphomolybdate, leading to secondary nucleation on the external surface. This secondary nucleation increases the thickness of the outer layer as the inner core is depleted, thus producing hollow sub-micron spheres as illustrated in Figure 8 (a). Similar behaviours have been observed for calcium carbonate by Yu et al., [26]. In some cases, low supersaturation rates and insufficient diffusion pathway produces filled sub-micron Cs-phosphomolybdate spheres, as illustrated in Figure 8(b).

Figure 9: Scanning electron images illustrating the formation of zirconium citratomolybdate, 192 hrs into the synthesis. The images were taken at different magnifications: (a) contact twinning at 29.63 K; (b) penetration twinning at 125.70 K.

Figure 9 provides images taken at 192 hrs into the synthesis where the formation of elongated Zr-citratomolybdate particles is seen. Figure 9(b) indicates a growth penetration twin at an angle. This occurs at a rotation axis, where it forms a new symmetry which results in a plane where the atoms are shared between the two crystals. Figure 9(a) indicates growth initiated

by multiple cyclical twinning. This is a type of contact twin where the compositional surfaces are not parallel during growth. A spherical ball is formed when the Zr-citratomolybdate particles have twinned along the dominating plane resulting in the branching behaviour. The branching occurs along the dominating axis and new nucleation events will result in the formation of complex structures with radiating growth mode from a central nucleus. There are many factors influencing the growth and the nucleation of the particles, which involve the solubility and acidity of the additive used.

Figure 10: Scanning electron images illustrating the formation of zirconium citratomolybdate, 336 hrs into the synthesis. The images were taken at different magnifications: (a) fully developed zirconium citratomolybate at 21.02 K; (b) step growth of crystals at 37.63 K.

Figure 10 shows a representative image at 336 hrs into the synthesis. It is evident from the SEM images the formation of the elongated particles has now occurred. Figure 10 (b) indicates crystal step growth. It is suggested for zirconium citratomolybdate synthesis that 336 hrs of reaction time is not a sufficient for 100% conversion. Further studies on crystal growth and the mechanisms are required to better understand this type of behaviour.

One of the assumptions, even at two weeks of reaction time, is that a significant amount of unconverted Cs-phosphomolybdate remains in the final product. The SEM image, shown in Figure 11, was taken after the full reaction time and is indicative of this, where a large amount of debris surrounding the Zr-citratomolybdate particles is evident. This assumption can be examined further using an elemental analysis, energy dispersive x-ray from the SEM.

Figure 11: Scanning electron microscope image used during electron dispersive spectroscopy analysis. The image illustrates zirconium citratomolybdate at 336 hrs into the synthesis. The EDX main parameters: working distance at 8 mm; electron intensity at 20 keV.

Figure 12: Electron dispersive spectroscopy point and identification method. The image illustrates the spectrum of specific locations of the sample (spectrum 2 and 3) and a mass spectrum of both locations.

In Figure 12, the EDX data taken at the marked locations in the SEM image shown in figure 11 are given. The EDX patterns highlight the presence of the expected atoms, with a predominance of Zr, Mo and O. The presence of C atoms, indicates the presence of citric acid. From the EDX pattern there is also evidence of Cs atoms, consistent with the unconverted Cs-phosphomolybdate. This can be further analysed by applying an EDX mapping technique as shown in Figure 13.

Figure 13: Electron-dispersive x-ray images displaying elemental mapping of zirconium citratomolybdate at 336 hrs. Images taken for several elements: (a) Zr Lα1; (b) Mo Lα1; (c) Cs Lα1.

As observed visually in Figure 13, there are large amounts of Zr and Mo atoms within the sample, most of which are in region of the cuboidal Zr-citratomolybdate particles. In contrast, the location of the Cs atoms is primarily within the debris around them, confirming that this is most likely unconverted Cs-phosphomolybdate. Using these SEM images, we conclude that the conversion is incomplete and yield relatively low.

3.4 Synthesis of zirconium citratomolybdate with Method 2

The initial approaches to the production of zirconium citratomolybdate involved the understanding of the chemistry within the system, relevant to both Methods 1 and 2. The final approach (Method 2) looked at controlling the feed rate of the reagents and induction time of the additive to increase the conversion of Cs-phosphomolybdate, due to the poor initial yield using Method 1 (as discussed in Section 3.3).

There were two main objectives for the synthesis optimisation; primarily, creating a batch of uniform elongated cuboidal shaped particles and a high yield. The optimised method involved a change in the following parameters

- Flow-rate of the additive
- Initial time of additive incorporation
- Washing of final batch

Taking the above into consideration, and the chemical influence of the additive, we have explored options for the optimization of this synthesis. Method 2 considers an increase of additive flow rate to 3.34 mL/min from 1.67 mL/min, altering the additive induction time to *t* = 30 mins from *t* = 0 mins, and addition of a $H_2CO_2NH_4$ washing step for Cs-phosphomolybdate dissolution, leading to the final conditions as discussed in this paper.

A proposed intermediate step (formation of citratomolybdate complex) in the $[ZrMo_2O_7(OH)_2] \cdot 2H_2O \cdot [(MoO_2)_2O(cit)_2]$ synthesis is expressed below.

$$Cs_3PMo_{12}O_{40} \cdot 14H_2O + 3HNO_3 \xrightarrow[90^oC]{} 6Mo_2O_5{}^{2+} + H_3PO_4 + 6H_2O \xrightarrow[Zr^{+}]{} 2\left[MoO_4{}^{2+}\right] + 2H_3cit^- \rightarrow [(MoO_2)_2O(cit)_2]^{6-} + 3H_2O \quad \text{Equation 5}$$

Equation 5 is based on the mechanism proposed by Alcock *et al.* [16]. As mentioned previously, it is the liberation of the molybdenum ions which drives the formation of Zr-molybdate. From the above equation, it is then the interaction between the molybdenum ions and the citric acid which controls the change in morphology to form the Zr-citratomolybdate.

Citric acid forms a complex with the molybdenum ion known as citratomolybdate [15-18]. It is this citratomolybdate complex which then adsorbs onto a surface of the molybdate particle inhibiting the growth on that particular surface, while the other surfaces continue to grow. This in turn results in the elongated, cuboidal shape. The angle of the Mo-O-Mo at 137^o [17] and the steric hindrance of the citric acid groups only allows the citratomolybdate complex to bind to specific faces. It is assumed the behaviour is due to the cis-arrangement of the two citric acid ligands, this prevents any binding to the concave side of the central Mo-O-Mo

bond. Understanding the production of the citratomolybdate complex is relevant to both Method 1 and 2 and thus the initial induction time of the citric acid additive at t = 0 mins was modified to t = 30 mins.

Implementation of Method 2 produced uniform batches of elongated Zr-citratomolybdate particles, SEM images are presented in Figure 14.

Figure 14: Scanning electron microscope images of synthesised zirconium citratomolybdate particles. Images are taken at different magnifications: (a) 1.90 K; (b) 3.16 K; (c) 6.74 K; (d) 25.05 K.

The SEM images in Figure 14 indicate consistent particles have been produced with no surrounding unconverted Cs-phosphomolybdate. The variation in magnification intensity (a-c) enables an overview of the batch and an enlarged image of an individual particle, and highlights any areas within the sample where debris could be present. From Figure 14 a), it is evident there is no unconverted Cs-phosphomolybdate present, even across a large sample, and the application of the optimised method proved to be successful.

A change of the additive feed, from 1.67 mL/min to 3.34 mL/min was also implemented. The increased feed rate results in the accumulation of the citrate ions above the critical supersaturation concentration, where growth of the crystal can occur. By increasing the feed rate, it enhances the interaction of the growth units of, in this case, the molybdenum and citrate ions. The initial method had a shorter nucleation period because the additive was insufficiently supplied. This maintained the solute concentration below the critical supersaturation concentration, and thus crystal growth was limited.

The initial time for addition of the citric acid was changed from t = 0 mins to t = 30 mins, as previously discussed in the methodology. This initial induction time period enables the interaction of the two growth units, $[Mo_2O_5]^{2+}$ and $[Zr]^{+}$, to nucleate Zr-molybdate. The delay

of citric acid incorporation, enables the interaction of citrate ions and $[Mo_2O_5]^{2+}$ to form the citratomolybdate complex which acts as an inhibitor on selective surfaces.

Collectively, the aim of increasing the feed rate and time delay of the additive was to increase the rate of reaction of the Zr-citratomolybdate particles with a high yield. Previous batches with the initial method produced poor yield ranging from 20% to 40%. However, implementing the new method enabled the production of 70% for a reaction time of 5 days. Indeed, due to equipment failure, the reaction did not have the full two weeks of conversion, although, from the results obtained it is most certain >~90% could have been achieved for the new method if it was run to completion.

The washing regime was prepared by separating the precipitated solids from the supernatant, via filtration, and then washed with 2 M ammonium carbamate, at a 2:1 ratio of washing agent to solids. This was left until the Cs-phosphomolybdate was fully dissolved (identified by the disappearance of the yellow colour) which required around 10 mins. The particles and the carbamate washing agent dispersion underwent a centrifugal separation at 3500 rpm for 10 mins. The supernatant was removed as waste and the solids were re-dispersed in 2 M nitric for neutralisation, for 30 mins. Centrifugal separation under the same conditions was implemented, at identical conditions, for phase separation of the particles and the nitric acid. After the supernatant was removed, the particles were placed in the oven for drying at 55^{o}C. During trials of washing on a small scale, SEM images were taken prior to the washing and after to determine the concentration of carbamate required and the time of the washing.

Ammonium carbamate was chosen for selective dissolution, based on research conducted by Jiang *et al.* [6]. This washing reagent is known to dissolve Cs-phosphomolybdate by hydrolysis of the Keggin phosphomolybdate anion (within the $Cs_3PMo_{12}O_{40} \cdot xH_2O$ structure),

to produce $[MoO_4]^{2-}$ and $[PO_4]^{3-}$ ions. The overall reaction proposed is expressed in Equation 6.

$$[PMo_{12}O_{40}]^{3-} + 12H_2O \rightarrow PO_4^{3-} + 12[MoO_4]^{2-} + 24H^+ \quad \text{Equation 6}$$

The initial breakdown of the keggin complex then leads to the production of ammonia and carbon dioxide. This takes place when the carbamate ions interact with hydrogen ions.

$$24H_2NCO_2^- + 24H^+ \rightarrow 24NH_3 + 24CO_2 \quad \text{Equation 7}$$

Carbamate is known to protonate and forms carbamic acid, which instantaneously decomposes into NH_3 and CO_2 gas. This is an effective washing reagent as smaller more soluble anions are formed and the liberation of CO_2 is known to drive the dissolution process under non-equilibrium conditions.

Dissolution of Zr-molybdate can also occur with ammonium carbamate. Jiang *et al* [6] assumed a dissolution model as expressed by Equation 8.

$$ZrMo_2O_7(OH)_2(H_2O)_2 \rightarrow Zr^{4+} + 2[MoO_4]^{2-} + 3H_2O \quad \text{Equation 8}$$

The breakdown of Zr-molybdate into zirconium and molybdate ions is followed by the interaction of carbamate ions with zirconium, to form a zirconium carbamate ($Zr(CO_3)_x^{4-2x}$) complex. This reaction is expressed by Equation 9.

$$Zr^{4+} + xCO_3^{2-} \rightarrow Zr(CO_3)_x^{4-2x} \quad \text{Equation 9}$$

It is the formation of the $Zr(CO_3)_x^{4-2x}$ complex which drives the dissolution process, where the rate of dissolution is however much slower than Cs-phosphomolybdate. It is governed by the thermodynamic energies, which are controlled by how different chemical bond types interact with the solvent. Cs-phosphomolybdate dissolution breaks down into smaller, soluble components and requires the protonation of the carbamate, whereas, Zr-molybdate requires

more energy for zirconium carbamate complex formation. Therefore, Zr-molybdate disintegrates into less soluble ions and the relative dissolution rate is much slower.

The washing procedure is a key step in the optimisation process for delivering a high quality uniform product. While the aim is to remove any unconverted Cs-phosphomolybdate it is clear that excessive washing with carbamate will also dissolve the zirconium complex, which is not desirable. Therefore the carbamate should be mixed for a limited amount of time. As an example, Figure 14 (d) illustrates the effect of exceeding the equilibrium washing time. The elongated Zr-citratomolybdate particle is surrounded by porous material; which can be assumed to be the initial stages of the dissolution process.

3.5 Crystalline structure of nuclear waste simulants

Interaction of x-rays with the Cs-phosphomolybdate, Zr-molybdate and Zr-citratomolybdate powders produced a clear diffraction pattern. Essentially, the fingerprint of each system has been determined through the PXRD technique. The crystal structure of Cs-phosphomolybdate is presented in Figure 15 and is identified to crystallise in a cubic lattice with a space group of *Pn3m*. The Hermann-Mauguin [27] space group notation suggests Cs-phosphomolybdate crystallises in a primitive lattice cell, denoted by P, this lattice contains a diagonal glide plane half a unit cell length in each direction, and a 3-fold symmetry with mirror plane (3m), along the cell edges. The lattice parameters also determined as $\alpha = \beta = \gamma = 90^o$ and $a = b = c = 11.79^o$.

Indexing of the peaks were derived using the lattice parameters, the wavelength of the radiation source and the calculation of d_{hkl}, a manual iterative method was used to estimate the 2θ position. The miller indices (*hkl*) were assigned corresponding to the 2θ position obtained from the XRD pattern.

Figure 15: X-ray diffraction pattern for caesium phosphomolybdate.

An example of this would be to explore a number of *hkl* values i.e. (100), (110), (111), (200) etc. Initial stages involve calculating the interplanar d-spacing, with respect to the crystal system. This is followed by applying the Bragg's law to determine the *2θ* position. For $hkl = (110)$,

$$\frac{1}{d_{110}^2} = \frac{1^2+1^2+0^2}{11.796^2} \rightarrow d_{110} = 8.34\dot{A} \qquad \text{Equation 10}$$

$$\sin\theta_{110} = \frac{1.54}{2(8.34)} \rightarrow 2\theta = 10.59^o \qquad \text{Equation 11}$$

The calculation corresponds to the first main peak of the structure. From Figure 15 it can be suggested that the main peaks are visible at 10.59^o (110), 18.40^o (211), 23.83^o (310), 26.14^o (222) and 30.27^o (400). The peaks in Figure 15 are in good correlation Cs-phosphomolybdate XRD reported by Bykhovskii *et al.*[7].

The Hermann-Mauguin space group notation for Zr-molybdate structure is $I4_1cd$, as determined by XRD. Figure 16 illustrates the XRD patterns for both Zr-molybdate and Zr-citratomolybdate, indicating matching structures and thus the crystallographic parameters remain *identical*. The incorporation of the citric acid additive has no direct effect on the crystal structure. The citratomolybdate complex attaches onto the specific surface and alters the rate of growth of that surface. It does not however change the atomic structure of a particular plane contained within the crystal.

The space group suggests a body centred tetragonal lattice structure, denoted by I. The object is repeated by the point group symmetry of 4/mm parallel to the c-axis. This is a 4-fold screw axis with an anticlockwise rotation of 90^o, the unit of rotation is 1/4c^o parallel to the c-axis.

Perpendicular to the a- and b-axis are the c-axial glide planes, with a unit translation of 1/2c^{o} in a direction parallel to the c-axis. Perpendicular to the directions 45^{o} from a- and b-axis and 90^{o} from the c-axis are the diamond glide planes, with a translation of 1/4a^{o}+1/4b^{o}+1/4c^{o}. The lattice parameters, also determined from XRD, as $\alpha = \beta = \gamma = 90^{o}$ and $a = b = 11.45\,\dot{A}$ and $c = 12.49\,\dot{A}$. Additionally, Figure 16 compares the XRD pattern of Zr-molybdate particles synthesised by Clearfield and Blessing [1] and again excellent agreement is seen to this previous reported data.

Figure 16: X-ray diffraction pattern for zirconium molybdate, zirconium citratomolybdate and a comparison to zirconium molybdate particles synthesised by Clearfield and Blessing.

From Figure 16 it can be suggested that the main peaks visible are 15.45^{o} (200), 21.03^{o} (202), 24.56^{o} (310) and 28.46^{o} (312). These peak indices correlate well with the work of Fourdrin *et al.* [28]. In contrast, the peak positions are at a slight shift compared to the XRD pattern from this previous study. The reason for this shift is due to the difference in radiation source, as Fourdrin *et al.* [28] employed Co-Kα radiation source, where $\lambda = 1.79\dot{A}$.

The diffraction patterns of Cs-phosphomolybdate and Zr-molybdate can be compared, where the size of the crystalline material relative to each other may be indicated. Large crystallites tend to give rise to narrow sharp peaks. Considering the SEM images and PSD data, the Cs-phosphomolybdate particles have a size peak of ~0.8 µm. This mean is compared to the Zr-molybdate particles, where the size peak mean value is between 3-4 µm. The XRD peaks of Cs-phosphomolybdate and Zr-molybdate suggest the peak width increases with decreasing particle size. However, it is important to consider that the peak width also increases as a result of variations in d-spacing caused by microstrain.

The number observed peaks is related to the symmetry of crystal. In the case of Zr-molybdate there are a large number peaks, indicating low symmetry (8 symmetry operators). The

intensities of the peaks relate to the type of atoms present on the planes. The scattering intensities for the x-rays are directly related to the number of electrons in the atom. It is known that that the lighter atoms scatter weak x-rays, whereas, heavy atoms scatter x-rays more effectively. The difference in atomic size directly correlates to the difference in interplanar spacing. Thus, in the case of Zr-molybdate the (2 0 0) plane may contain of Zr and Mo atoms and for Cs-phosphomolybdate structures the (2 2 2) plane contains Cs atoms.

As discussed, the XRD patterns for both caesium and zirconium compounds closely align with previously published research [1, 7] where it has been generally established that synthesised solids are contained in single crystallised phases. Other complimentary techniques have also previously been studied, including Raman spectroscopy and multi-element NMR to help identify crystal structure [1, 6-8, 28]. In particular, Jiang *et al.* [6] studied the dissolution of Cs-phosphomolybdate and Zr-molybdate with Raman spectroscopy, informing the presence of MoO_4^{2-}(identified by the Mo-O bond stretch at 896 cm^{-1}) and $[PMo_{12}O_{40}]^{3-}$, which were further confirmed by ^{31}P NMR studies. Due the close correlation with this preceding literature, and in addition, the well-defined peaks in the XRD patterns (Figures 15 & 16), it is concluded that at least the majority of solids have crystallised into single structures for each of the caesium and zirconium species, and if any amorphous phases exist at all, they are only minor. However, it has been identified that selected-area electron diffraction (TEM) could indicate the degree of crystallinity and phase of individual particles, and future work will look to confirm any presence of non-crystalline solids in the final products.

This study focuses on the synthesis of non-active nuclear waste particles, it is therefore of further interest to understand their formation under continuous irradiation and thus, the influence of the radiolysis products. Reprocessing of nuclear waste is conducted in highly

acidic environments, where radiolysis products such as NO_x, and potentially the primary radiolysis products of water, hydrogen peroxide (H_2O_2) are liberated. A number of studies have been conducted to understand the radiolysis of nitric acid [29-31] and the decomposition of H_2O_2 under continuous irradiation conditions to liberate O_2 [32]. It is the radiolysis products that are redox active which can readily interact with transition metals, in this particular case Zr and Mo ions, to alter their oxidation state. It is believed the change in oxidation state of the metal species leads to a decrease in solubility and thus provides additional nucleation sites for particle growth. Any presence of O_2 in solution can also accelerate particle growth due to the drive in equilibrium to favour the formation of intermediates with nucleation sites. Thus, under induced irradiated conditions, the nuclear waste particle size and morphology may be influenced by the redox conditions of the radiolysis products at the solid-liquid interface, as reported by Alrehaily *et al.* [33] on the formation of cobalt oxide under γ-radiation. It is possible to hypothesis on the influence of radiolysis products under the same process conditions as discussed in the study. It is thought they may increase the aspect ratio of Zr-citratomolybdate particles, as the change in the solution Zr and Mo properties accelerate the rate of particle formation. This topic of interest will be investigated in further research.

Conclusions

This paper highlights key components related to the synthesis, morphology modification and particle characterisation of highly active nuclear waste simulants. The reaction precipitation method enabled the production of caesium phosphomolybdate, zirconium molybdate and zirconium citratomolybdate particles on a relatively large scale.

Manipulation of morphology (by addition of citric acid) produced particles with identical chemical structures, although different shape. The key difference is the transformation of the aspect ratio, from ~1 for cubic Zr-molybdate particles to ~8 for the elongated Zr-citratomolybdate particles. Process parameters such as decreasing the flow rate, modifying additive induction time and particle washing with ammonium cabamate enabled the production of high yield and uniform particles. Implementing particle characterisation techniques such as SEM and EDX during synthesis and post-synthesis, also confirmed the presence of unconverted Cs-phosphomolybdate at the end of the Method 1 synthesis route.

A chemical mechanism has been proposed for the initial production of spherical Cs-phosphomolybdate to cubic Zr-molybdate and finally elongated-cuboidal Zr-citratomolybdate particles. It is the liberation of the oxomolybdate complex, $[MoO_5]^{2+}$, which determines the overall yield of the final product. Ultimately, this research provides fundamental understanding for further particle and dispersion characterisation, which can be directly utilised for improvements in the nuclear waste treatment process.

Acknowledgements

We would like to thank Sellafield Ltd. and National Nuclear Laboratory (NNL) for carrying out experiments within their laboratories, and the Engineering and Physical Sciences Research Council (EPSRC) funding for this research.

References

[1] A. Clearfield and R.H. Blessing, J. Inorg. Nucl. Chem., 34 (1972) 2643-2663.
[2] L. Xuegang, C. Jin, Z. Yanchao, and W. Jianchen, Procedia Chem., 7 (2012) 575-580.
[3] F. Prinetto, G. Cerrato, G. Ghiotti, A. Chiorino, M.C. Campa, D. Gazzoli, and V. Indovina, J. Phys. Chem., 99 (1995) 5556-5567.
[4] F. Monroy-Guzmán, L.V. Díaz-Archundia, and A. Contreras Ramírez, Appl. Radiat. Isotopes, 59 (2003) 27-34.
[5] F.J. Doucet, D.T. Goddard, C.M. Taylor, I.S. Denniss, S.M. Hutchison, and N.D. Bryan, Phys. Chem. Chem. Phys., 4 (2002) 3491-3499.
[6] J. Jiang, I. May, M. Sarsfield, M. Ogden, D. Fox, C. Jones, and P. Mayhew, J. Solution Chem., 34 (2005) 443-468.

[7] D.N. Bykhovskii, T.I. Kol'tsova, and M.A. Kuz'mina, Radiochemistry, 48 (2006) 429-433.
[8] A. Magnaldo, M. Masson, and R. Champion, Chem. Eng. Sci., 62 (2007) 766-774.
[9] F. Monroy-Guzman, L.V. Díaz-Archundia, and S. Hernández-Cortés, J. Brazil. Chem. Soc., 19 (2008) 380-388.
[10] F. Monroy-Guzman, T. Rivero Gutiérrez, I.Z. López Malpica, S. Hernández Cortes, P. Rojas Nava, J.C. Vazquez Maldonado, and A. Vazquez, Appl. Radiat. Isotopes, 70 (2012) 103-111.
[11] S. Kumar, M. Sivaiah, K. Venkatesan, R. Krishna, G. Murthy, and P. Sasidhar, J. Radioanal. Nucl. Chem., 258 (2003) 321-327.
[12] C. Lind, D.G. VanDerveer, A.P. Wilkinson, J. Chen, M.T. Vaughan, and D.J. Weidner, Chem. Mater., 13 (2001) 487-490.
[13] J.S.O. Evans, J. Chem. Soc., Dalton Trans., (1999) 3317-3326.
[14] M.S. Vukasovich and J.P.G. Farr, Polyhedron, 5 (1986) 551-559.
[15] A. Samotus, A. Kanas, M. Dudek, R. Gryboś, and E. Hodorowicz, Transit. Metal Chem., 16 (1991) 495-499.
[16] N.W. Alcock, M. Dudek, R. Grybos, E. Hodorowicz, A. Kanas, and A. Samotus, J. Chem. Soc. Dalton Trans., (1990) 707-711.
[17] Z.-H. Zhou, H.-L. Wan, and K.-R. Tsai, Polyhedron, 16 (1997) 75-79.
[18] J.J. Cruywagen, E.A. Rohwer, and G.F.S. Wessels, Polyhedron, 14 (1995) 3481-3493.
[19] R.W. Cahn, Adv. Phys., 3 (1954) 363-445.
[20] B.G. Wang, E.W. Shi, and W.Z. Zhong, Cryst. Res. Technol., 33 (1998) 937-941.
[21] M.A. Jaswon and D.B. Dove, Acta Crystallogr., 9 (1956) 621-626.
[22] S. Eiden and G. Maret, J. Colloid. Interf. Sci., 250 (2002) 281-284.
[23] H. Cölfen, Macromol. Rapid Comm., 22 (2001) 219-252.
[24] H.G. Yang and H.C. Zeng, J. Phys. Chem. B, 108 (2004) 3492-3495.
[25] J. Hu, M. Chen, X. Fang, and L. Wu, Chem. Soc. Rev., 40 (2011) 5472-5491.
[26] J.G. Yu, H. Guo, S.A. Davis, and S. Mann, Adv. Funct. Mater., 16 (2006) 2035-2041.
[27] T. Hahn, International Tables for Crystallography, Space-Group Symmetry, Wiley, 2005.
[28] C. Fourdrin, S. Esnouf, V. Dauvois, J.P. Renault, L. Venault, M. Tabarant, D. Durand, A. Chenière, C. Lamouroux-Lucas, and F. Cochin, J. Nucl. Mater., 426 (2012) 38-44.
[29] P.K. Bhattacharyya and R.D. Saini, Int. J. Radiat. Phys. Chem., 5 (1973) 91-99.
[30] P.-Y. Jiang, R. Nagaishi, T. Yotsuyanagi, Y. Katsumura, and K. Ishigure, J. Chem. Soc., Faraday Trans., 90 (1994) 93-95.
[31] R. Nagaishi, Radiat. Phys. Chem., 60 (2001) 369-375.
[32] E. Hayon, T. Faraday Soc., 60 (1963) 1059-1067.
[33] L.M. Alrehaily, J.M. Joseph, M.C. Biesinger, D.A. Guzonas, and J.C. Wren, Phys. Chem. Chem. Phys., 15 (2013) 1014-1024.

Figure 2: A 4 L Batch reactor vessel set-up for caesium phosphomolybdate, zirconium molybdate and zirconium citratomolybdate synthesis. The reactor vessel is a jacketed vessel (containing silicon oil for heating purposes) an overhead paddle agitator, a condenser with circulating water at 5^{o}C and a temperature probe.

Figure 2: Schematic illustration of the synthesis steps for caesium phosphomolybdate and zirconium molybdate particle production.

Figure 3: A schematic of method 1 illustrating the synthesis steps required for morphological modification of zirconium molybdate to produce zirconium citratomolybdate particles with incorporation of citric acid.

Figure 4: Schematic of Method 2 illustrating the synthesis steps require for morphological transformation of zirconium molybdate to zirconium citratomolybdate with incorporation of citric acid.

Figure 5: Scanning electron microscope images of synthesised caesium phosphomolybdate particles. Images are taken at different magnifications: (a) 23.01 K; (b) 23.25 K ; (c) 29.32 K; (d) 151.09 K .

Figure 6: Proposed aggregation mechanism for caesium phosphomolybdate particles. Stage 1: formation of the nanocrystallites; Stage 2: formation of the primary aggregates, consisting of cemented nanocrystallites; Stage 3: formation of the secondary aggregate, consisting of the submicron aggregates

Figure 7: Scanning electron microscope images of synthesised zirconium molybdate particles. Images are taken at different magnifications: (a) 1.74 K; (b) 7.79 K; (c) 19.66 K; (d) 27.99 K.

Figure 8: Scanning electron images illustrating the breakdown of caesium phosphomolybdate, 24 hrs into the synthesis. The images were taken at different magnifications: (a) hollow centre crystal at 130.56 K; (b) filled centre crystal at 152.60 K.

Figure 9: Scanning electron images illustrating the formation of zirconium citratomolybdate, 192 hrs into the synthesis. The images were taken at different magnifications: (a) contact twinning at 29.63 K; (b) penetration twinning at 125.70 K.

Figure 10: Scanning electron images illustrating the formation of zirconium citratomolybdate, 336 hrs into the synthesis. The images were taken at different magnifications: (a) fully developed zirconium citratomolybate at 21.02 K; (b) step growth of crystals at 37.63 K.

Figure 11: Scanning electron microscope image used during electron dispersive spectroscopy analysis. The image illustrates zirconium citratomolybdate at 336 hrs into the synthesis. The EDX main parameters: working distance at 8 mm; electron intensity at 20 keV.

Figure 12: Electron dispersive spectroscopy point and identification method. The image illustrates the spectrum of specific locations of the sample (spectrum 2 and 3) and a mass spectrum of both locations.

Figure 13: Electron-dispersive x-ray images displaying elemental mapping of zirconium citratomolybdate at 336 hrs. Images taken for several elements: (a) Zr Lα1; (b) Mo Lα1; (c) Cs Lα1.

Figure 14: Scanning electron microscope images of synthesised zirconium citratomolybdate particles. Images are taken at different magnifications: (a) 1.90 K; (b) 3.16 K; (c) 6.74 K; (d) 25.05 K.

Figure 15: X-ray diffraction pattern for caesium phosphomolybdate.

Figure 16: X-ray diffraction pattern for zirconium molybdate, zirconium citratomolybdate and a comparison to zirconium molybdate particles synthesised by Clearfield and Blessing.

Figure 1 4L batch reactor vessel set-up for CPM, ZM and ZMCA synthesis. The reactor vessel is a jacketed vessel contained silicon oil for heating purposes, an overhead paddle agitator, a condenser with circulating water at 5^{o}C and a temperature probe.

Figure 2 A schematic illustrating the synthesis steps for CPM and ZM particle formation.

Figure 3 A schematic of method 1 illustrating the synthesis steps required for morphological modification of ZM to produce ZMCA particles with incorporation of citric acid.

Figure 4 A schematic of method 2 illustrating the synthesis steps required for morphological modification of ZM to produce ZMCA particles with incorporation of citric acid.

Figure 5 Scanning electron microscope images of synthesised caesium phosphomolybdate particles. Images are taken at different magnifications: (a) 23.01 K; (b) 23.25 K ; (c) 29.32 K; (d) 151.09 K .

Figure 6 Proposed aggregation mechanism for caesium phosphomolybdate particles. Stage 1: formation of the nanocrystallites; Stage 2: formation of the primary aggregates, consisting of cemented nanocrystallites; Stage 3: formation of the secondary aggregate, consisting of the submicron aggregates

Figure 7 Scanning electron microscope images of synthesised zirconium molybdate particles. Images are taken at different magnifications: (a) 1.74 K; (b) 7.79 K; (c) 19.66 K; (d) 27.99 K.

Figure 8 Scanning electron images illustrating the breakdown of caesium phosphomolybdate, 24 hrs into the synthesis. The images were taken at different magnifications: (a) hollow centre crystal at 130.56 K; (b) filled centre crystal at 152.60 K.

Figure 9 Scanning electron images illustrating the formation of zirconium citratomolybdate, 192 hrs into the synthesis. The images were taken at different magnifications: (a) contact twinning at 29.63 K; (b) penetration twinning at 125.70 K.

Figure 10 Scanning electron images illustrating the formation of zirconium citratomolybdate, 336 hrs into the synthesis. The images were taken at different

magnifications: (a) fully developed zirconium citratomolybate at 21.02 K; (b) step growth of crystals at 37.63 K.

Figure 11 Scanning electron microscope image used during electron dispersive spectroscopy analysis. The image illustrates zirconium citratomolybdate at 336 hrs into the synthesis. The EDX main parameters: working distance at 8 mm; electron intensity at 20 keV.

Figure 12 Electron dispersive spectroscopy point and identification method. The image illustrates the spectrum of specific locations of the sample (spectrum 2 and 3) and a mass spectrum of both locations.

Figure 13 Electron-dispersive x-ray images displaying elemental mapping of zirconium citratomolybdate at 336 hrs. Images taken for several elements: (a) Zr Lα1; (b) Mo Lα1; (c) Cs Lα1.

Figure 14 Scanning electron microscope images of synthesised zirconium citratomolybdate particles. Images are taken at different magnifications: (a) 1.90 K; (b) 3.16 K; (c) 6.74 K; (d) 25.05 K.

Figure 15 X-ray diffraction pattern for caesium phosphomolybdate (CPM)

Figure 16 X-ray diffraction pattern for zirconium molybdate (ZM), zirconium citratomolybdate (ZMCA) and a comparison to zirconium molybdate particles synthesised by Clearfield and Blessing.

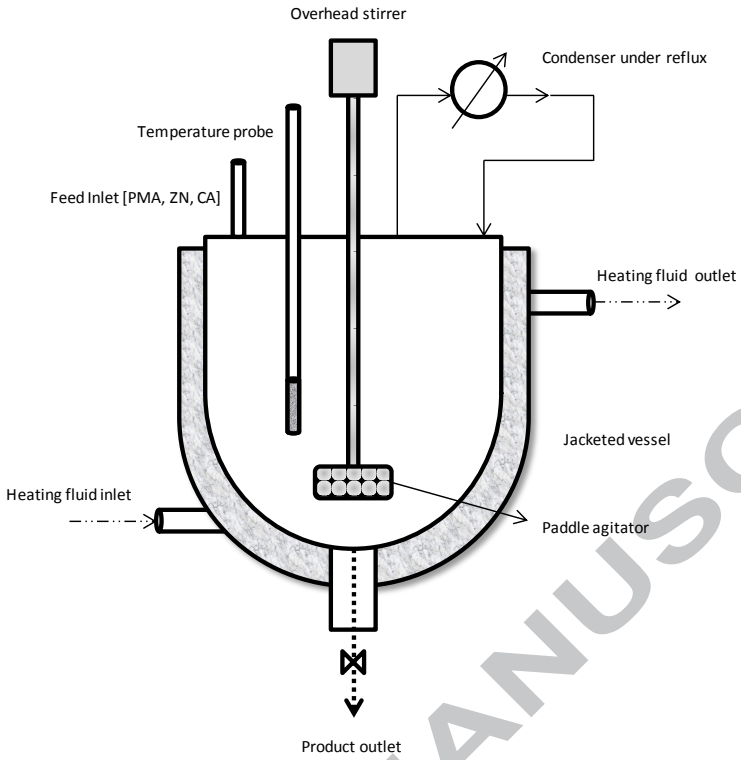

Figure 1

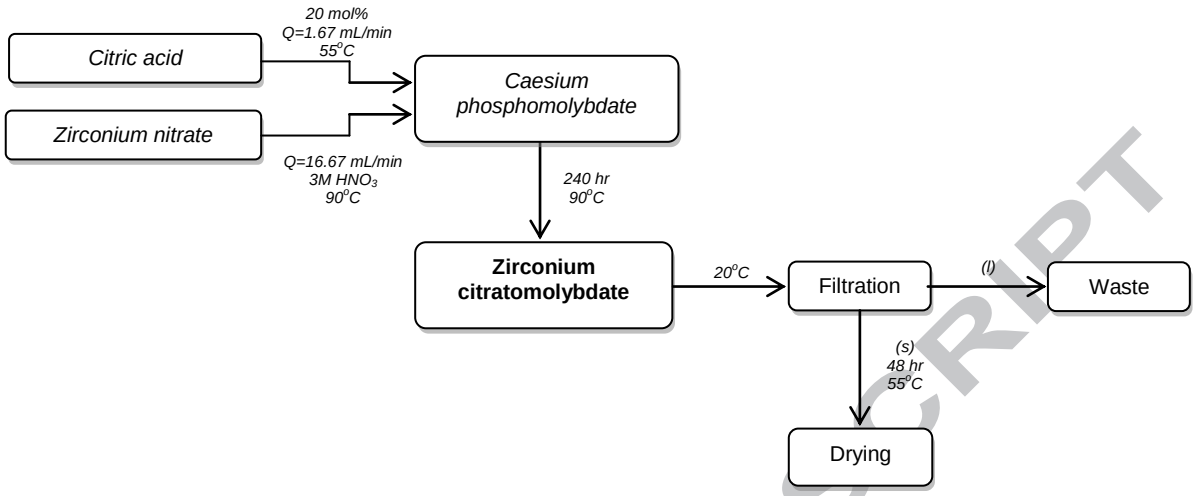

Figure 3

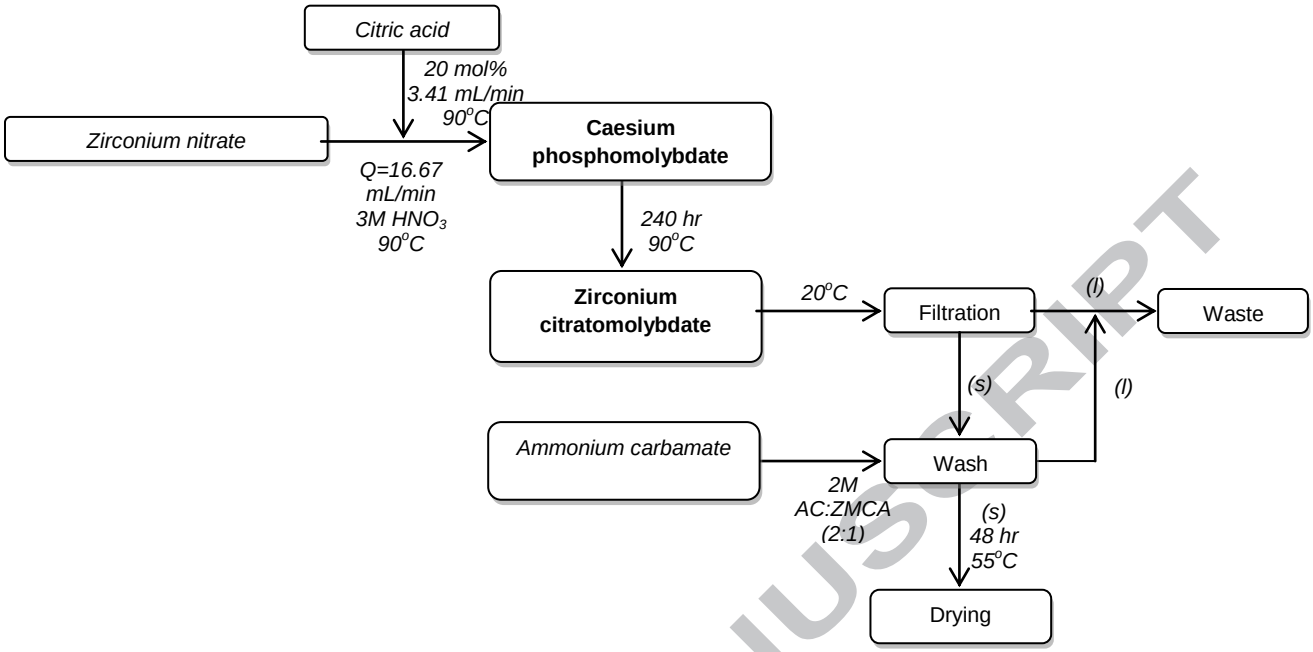

Figure 4

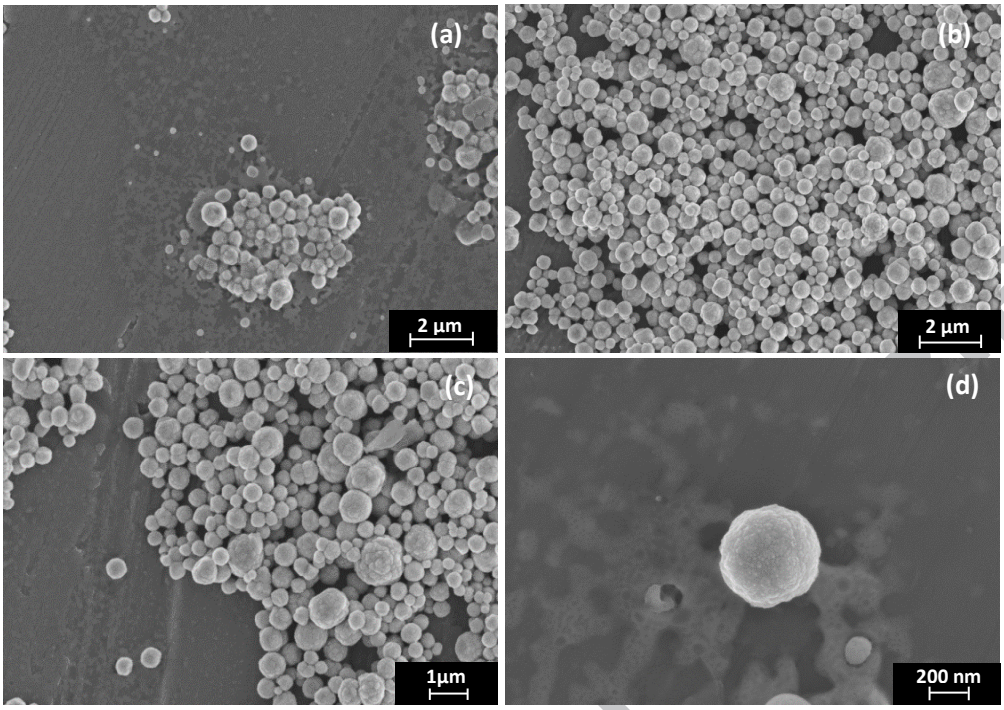

Figure 5

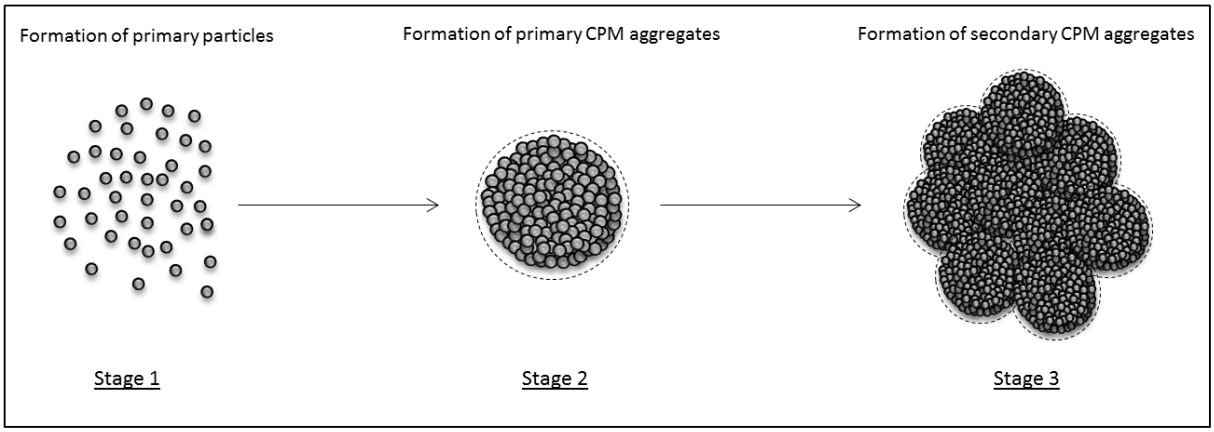

Figure 6

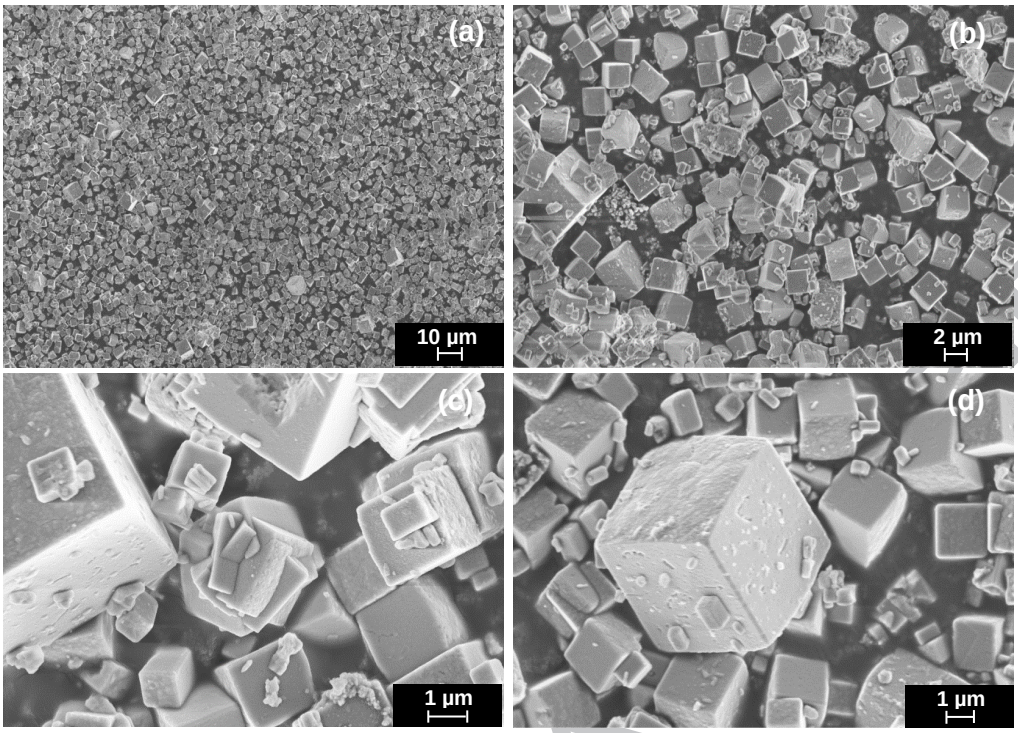

Figure 7

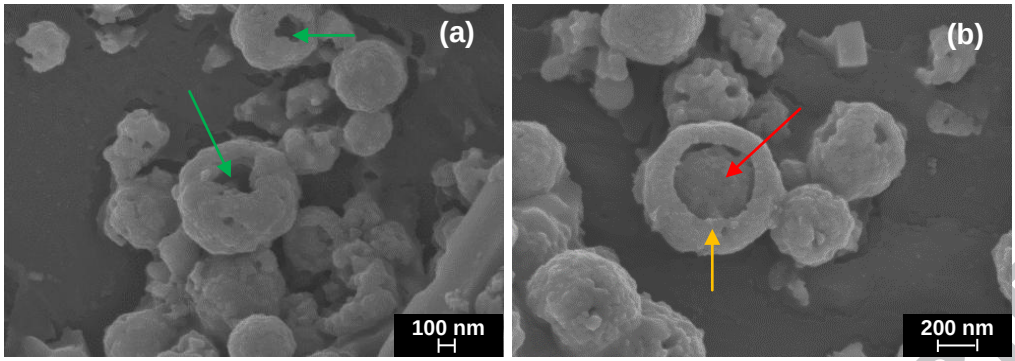

Figure 8

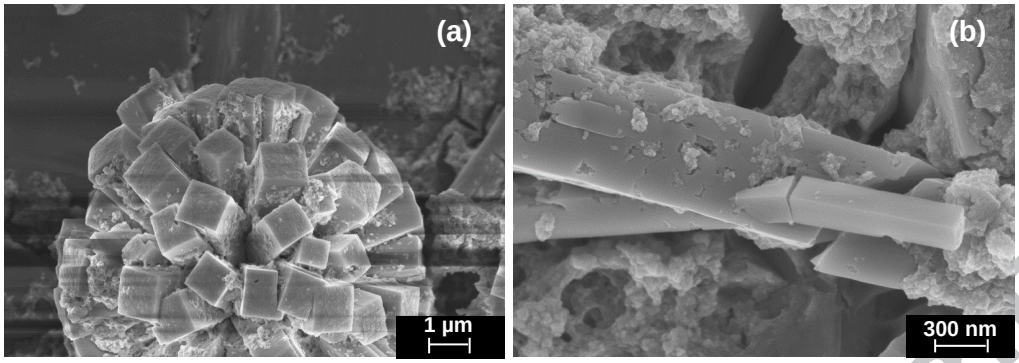

Figure 9

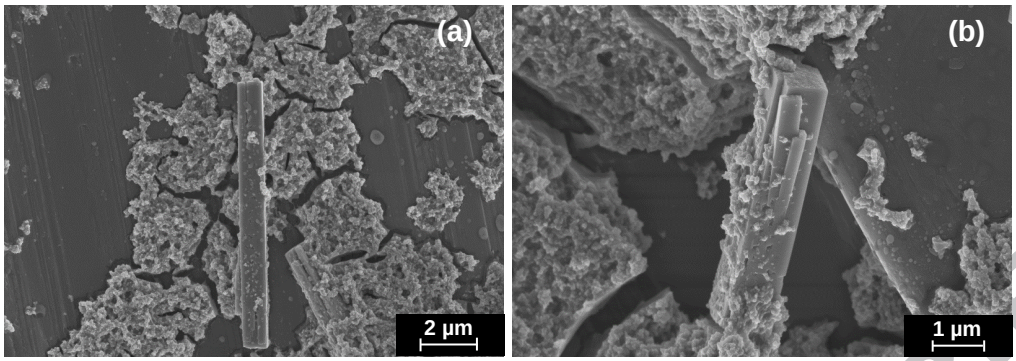

Figure 10

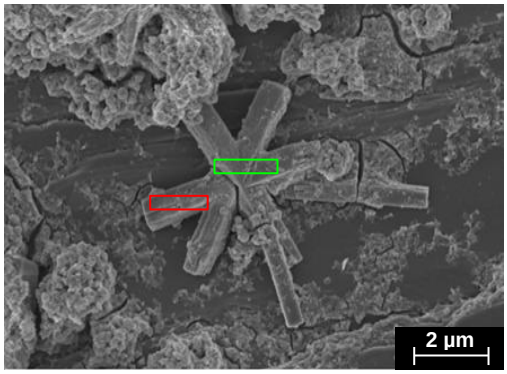

Figure 11

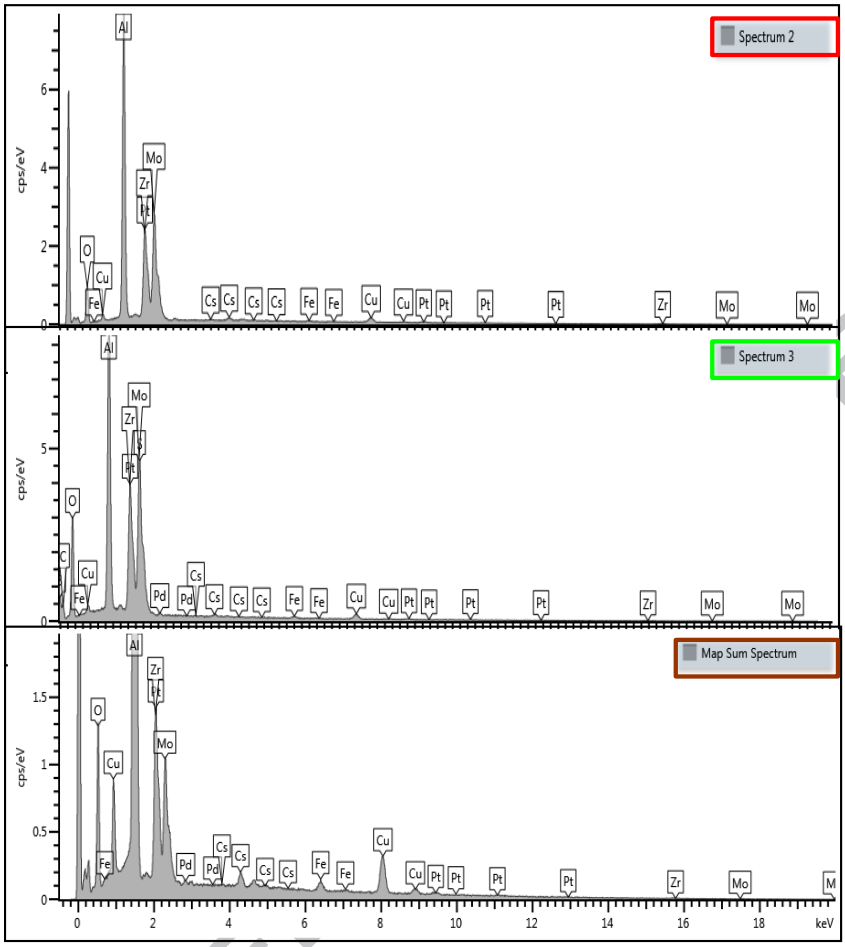

Figure 11

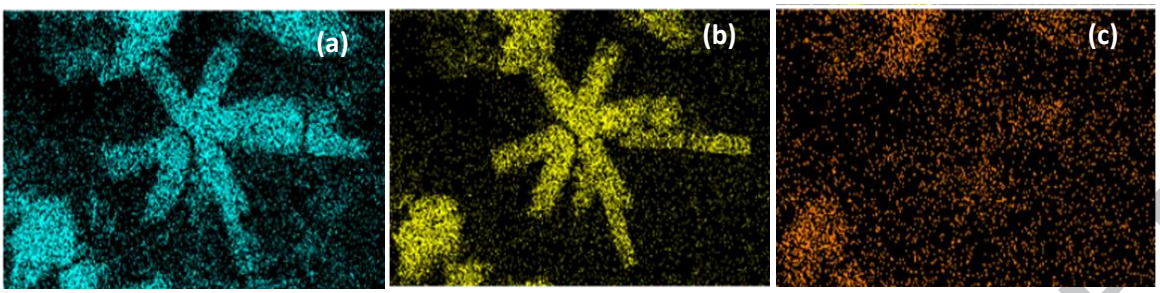

Figure 13

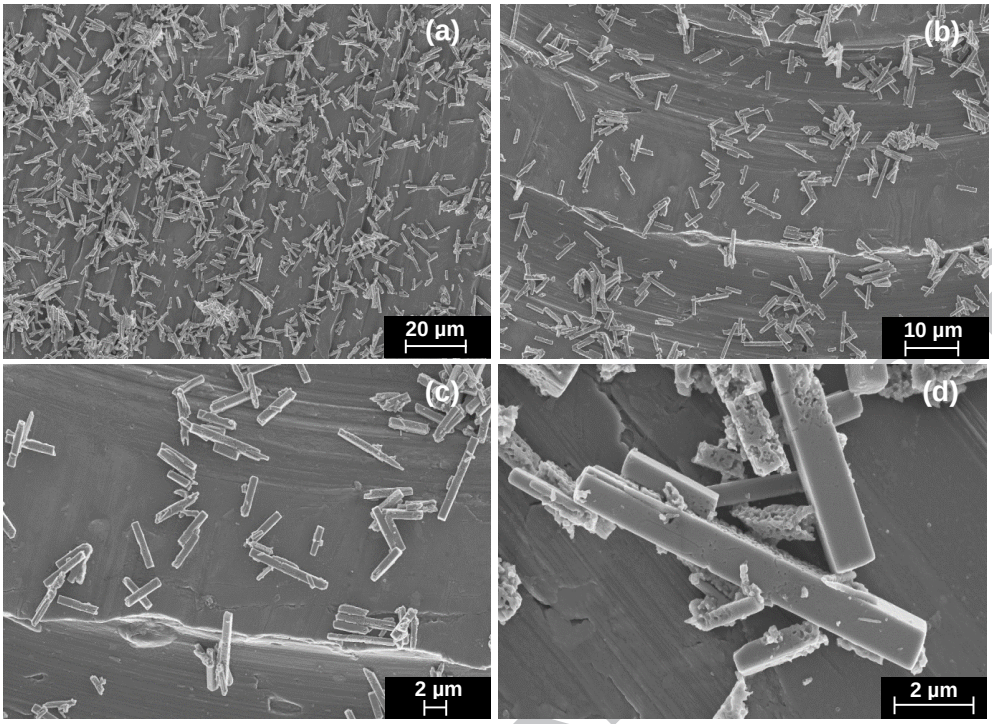

Figure 14

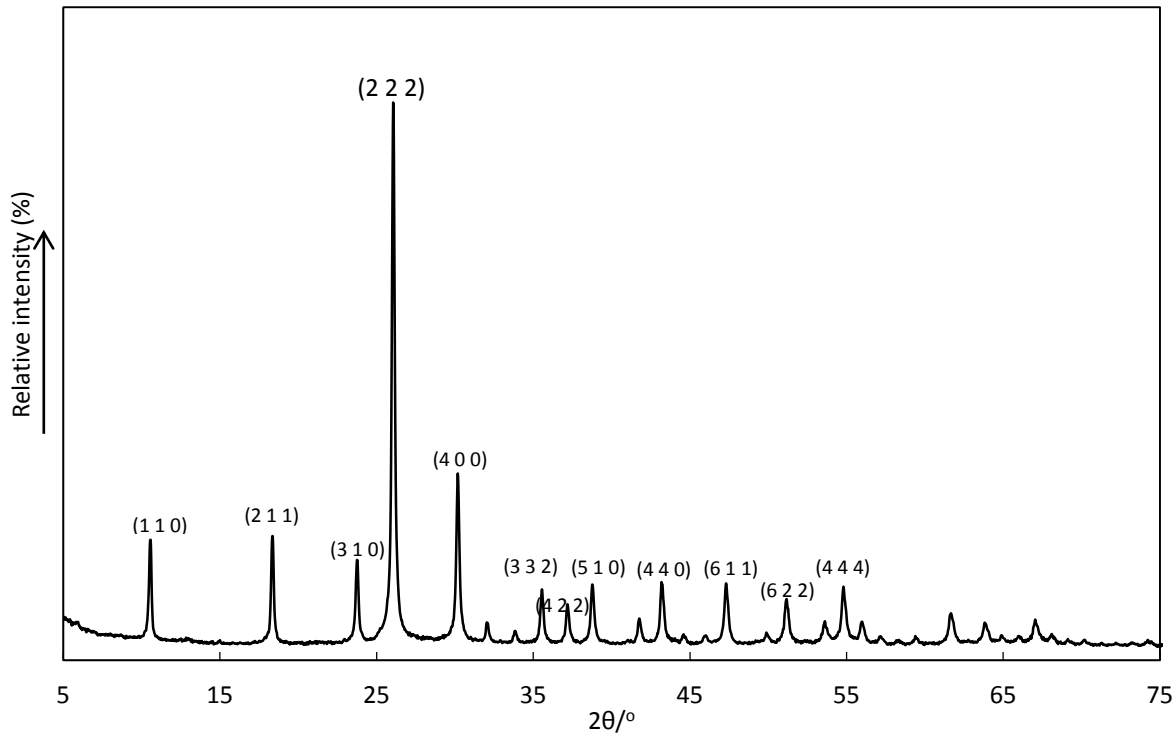

Figure 15

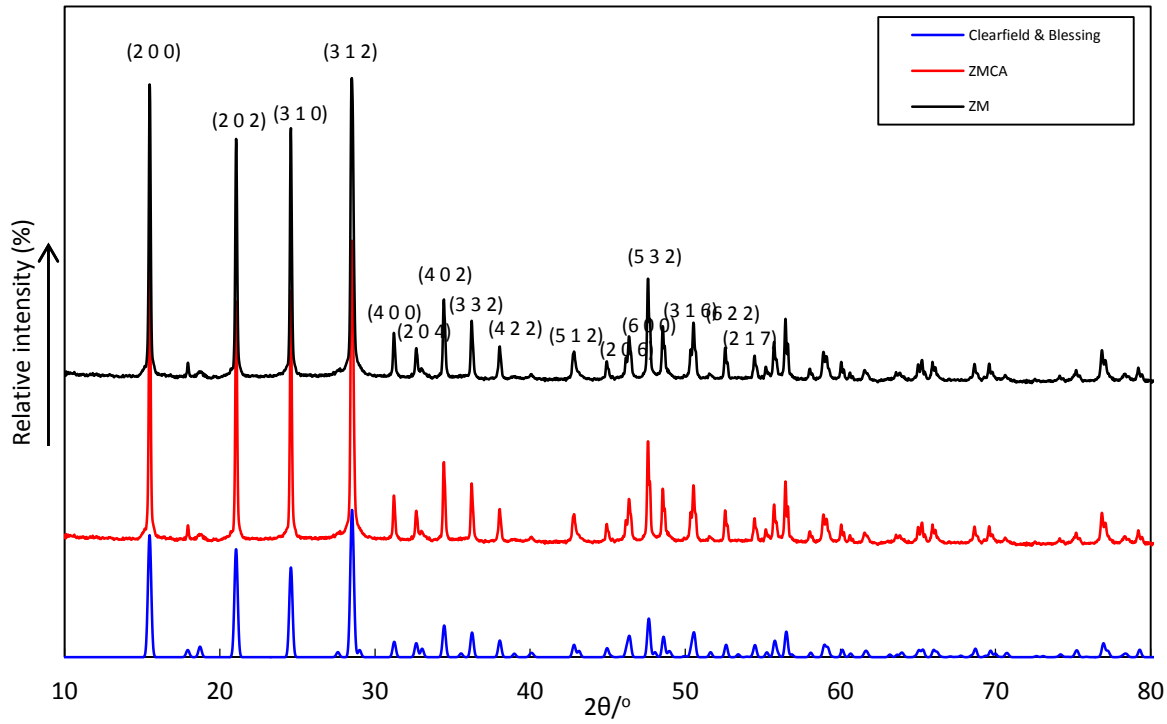

Figure 16

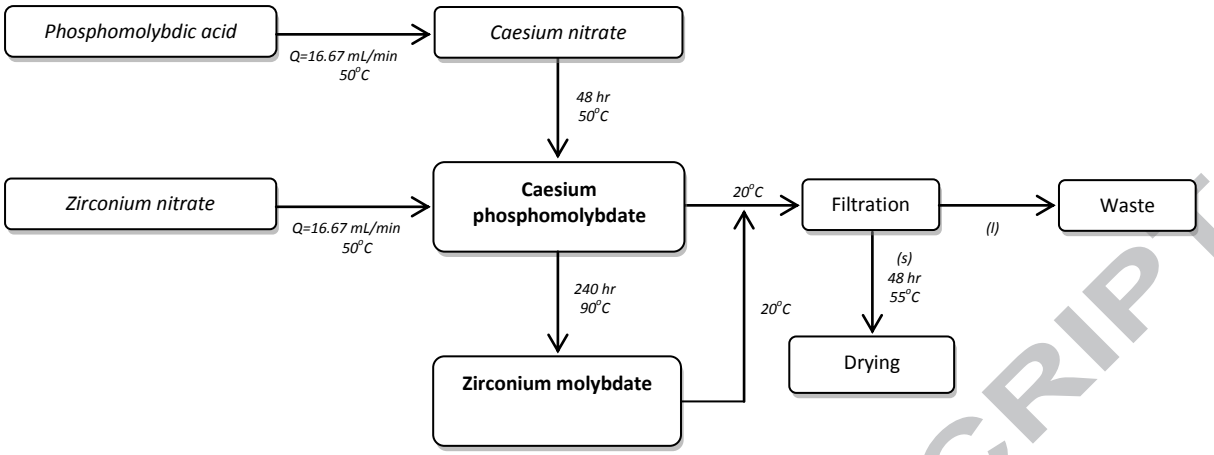

Figure 2

Abstract

Caesium phosphomolybdate ($Cs_3PMo_{12}O_{40} \cdot xH_2O$) and zirconium molybdate ($[ZrMo_2O_7(OH)_2] \cdot 2H_2O$) solids are known to precipitate out from highly active liquors (HAL) during reprocessing of spent nuclear fuel. Here, a new synthesis for these simulants is reported; with the initial step producing spherical ceasium phosphomolybdate particles, which can then be converted into cubic Zirconium molybdate. Additionally, the addition of citric acid prior to the formation of the zirconium salt is investigated. In this case, a citratomolybdate complex is generated, leading to the synthesis of elongated cuboidal zirconium citratomolybdate ($[ZrMo_2O_7(OH)_2] \cdot 2H_2O \cdot [(MoO_2)_2O(cit)_2]$). A key focus of this study is to explore the optimisation of reaction conditions to create a controlled environment for the particles to form with high conversion rates and with desired shape properties. Elemental and structural characterisation of the particles at various points during the synthesis, as well as post-synthesis, was undertaken to provide further insights. Ultimately, it is of importance to determine the mechanism of how these simulants are formed within the components in HAL. Establishing the influence of particle properties on HAL behaviour is key for current processing, post operational clean out (POCO) and life-time assessment of the nuclear waste facilities.